

Weyl-like points from band inversions of spin-polarised surface states in NbGeSb

I. Marković,^{1,2} C. A. Hooley,¹ O. J. Clark,¹ F. Mazzola,¹ M. D. Watson,¹ J. M. Riley,¹ K. Volckaert,¹ K. Underwood,¹ M. S. Dyer,³ P. A. E. Murgatroyd,⁴ K. J. Murphy,⁴ P. Le Fèvre,⁵ F. Bertran,⁵ J. Fujii,⁶ I. Vobornik,⁶ S. Wu,⁷ T. Okuda,⁸ J. Alaria,⁴ and P. D. C. King^{1,*}

¹*SUPA, School of Physics and Astronomy,
University of St Andrews, St Andrews KY16 9SS, United Kingdom*

²*Max Planck Institute for Chemical Physics of Solids,
Nöthnitzer Strasse 40, 01187 Dresden, Germany*

³*Department of Chemistry, University of Liverpool,
Liverpool L69 7ZD, United Kingdom*

⁴*Department of Physics, University of Liverpool,
Liverpool L69 7ZE, United Kingdom*

⁵*Synchrotron SOLEIL, CNRS-CEA, L'Orme des Merisiers,
Saint-Aubin-BP48, 91192 Gif-sur-Yvette, France*

⁶*Istituto Officina dei Materiali (IOM)-CNR,
Laboratorio TASC, Area Science Park,
S.S.14, Km 163.5, 34149 Trieste, Italy*

⁷*Graduate School of Science, Hiroshima University,
1-3-1 Kagamiyama, Higashi-Hiroshima 739-8526, Japan*

⁸*Hiroshima Synchrotron Radiation Center,
Hiroshima University, 2-313 Kagamiyama,
Higashi-Hiroshima 739-0046, Japan*

(Dated: November 21, 2019)

Abstract

Band inversions are key to stabilising a variety of novel electronic states in solids, from topological surface states in inverted bulk band gaps of topological insulators to the formation of symmetry-protected three-dimensional Dirac and Weyl points and nodal-line semimetals. Here, we create a band inversion not of bulk states, but rather between manifolds of surface states. We realise this by aliovalent substitution of Nb for Zr and Sb for S in the ZrSiS family of nonsymmorphic semimetals. Using angle-resolved photoemission and density-functional theory, we show how two pairs of surface states, known from ZrSiS, are driven to intersect each other in the vicinity of the Fermi level in NbGeSb, as well as to develop pronounced spin-orbit mediated spin splittings. We demonstrate how mirror symmetry leads to protected crossing points in the resulting spin-orbital entangled surface band structure, thereby stabilising surface state analogues of three-dimensional Weyl points. More generally, our observations suggest new opportunities for engineering topologically and symmetry-protected states via band inversions of surface states.

* To whom correspondence should be addressed: philip.king@st-andrews.ac.uk

1 INTRODUCTION

2 The routes by which different underlying symmetries can lead to a variety of topologi-
3 cally protected electronic states in solids have garnered great attention in the past years¹⁻⁵.
4 ZrSiS⁶, for example, has recently been established as a bulk Dirac nodal line system⁷⁻¹⁶,
5 with multiple lines of Dirac points protected by its nonsymmorphic and mirror crystalline
6 symmetries.^{4,7,17-19} When its nonsymmorphic symmetry is broken at the crystal surface,
7 new sets of electronic states are created, split off from the bulk manifold⁸. One such surface
8 state, SS, of dominantly Zr character, intersects the Fermi level (E_F), while another, SS',
9 of predominantly S character, is located at much higher binding energies^{8,20}. The existence
10 of these surface states is a result of very general symmetry considerations⁸, and so should
11 be expected to be ubiquitous across this materials class. It is still possible to tune their
12 properties, however. For example, isovalent replacement of Zr by the heavier Hf atom leads
13 to a similar set of surface states, but with the Hf-derived state developing a moderate spin
14 splitting as a result of its larger spin-orbit coupling^{9,21}.

15 Here, we employ aliovalent substitution in order to make a more dramatic modification
16 of the surface state spectrum, ultimately realising a surface band inversion. To this end, we
17 synthesised single crystals of a little-studied nonsymmorphic compound NbGeSb^{22,23} (see
18 Methods). NbGeSb is isostructural to ZrSiS. As shown in Fig. 1(c), it contains square nets
19 of Ge atoms in the ab plane, with two Nb layers and two Sb layers located between each pair
20 of neighbouring Ge planes. The atomic positions within each pair of Nb or Sb layers are
21 related to each other via a combined mirror reflection and translation by a fraction of the
22 unit cell, making the symmetry group of this structure nonsymmorphic. NbGeSb shares the
23 same total charge count as ZrSiS, and should therefore retain charge compensation between
24 electron- and hole-like carriers²⁴. However, Sb has one less valence electron than S, while Nb
25 has one more than Zr. A pronounced change in the relative positions and occupations of the
26 underlying electronic states can thus be expected as compared to ZrSiS. The SS surface state,
27 which forms a small electron pocket around \bar{X} in ZrSiS⁷⁻⁹, should become more electron-
28 doped in NbGeSb, thus being pushed down in energy. Moreover, SS', which is located more
29 than 1.5 eV below the Fermi level at the \bar{X} point in ZrSiS⁷⁻⁹, would be expected to become
30 hole-doped, thus being raised up to intersect the Fermi level in the vicinity of \bar{X} .

31 **RESULTS**

32 **Spin-split surface states of NbGeSb**

33 Fig. 1 illustrates how the above expectation is borne out in reality. Comparison of our
 34 angle-resolved photoemission (ARPES) measurements (Fig. 1(a)) with density-functional
 35 theory (DFT) supercell calculations (Fig. 1(b)) allows us to identify both the SS and SS'
 36 manifolds of surface states in NbGeSb. Both are clearly resolved where they disperse through

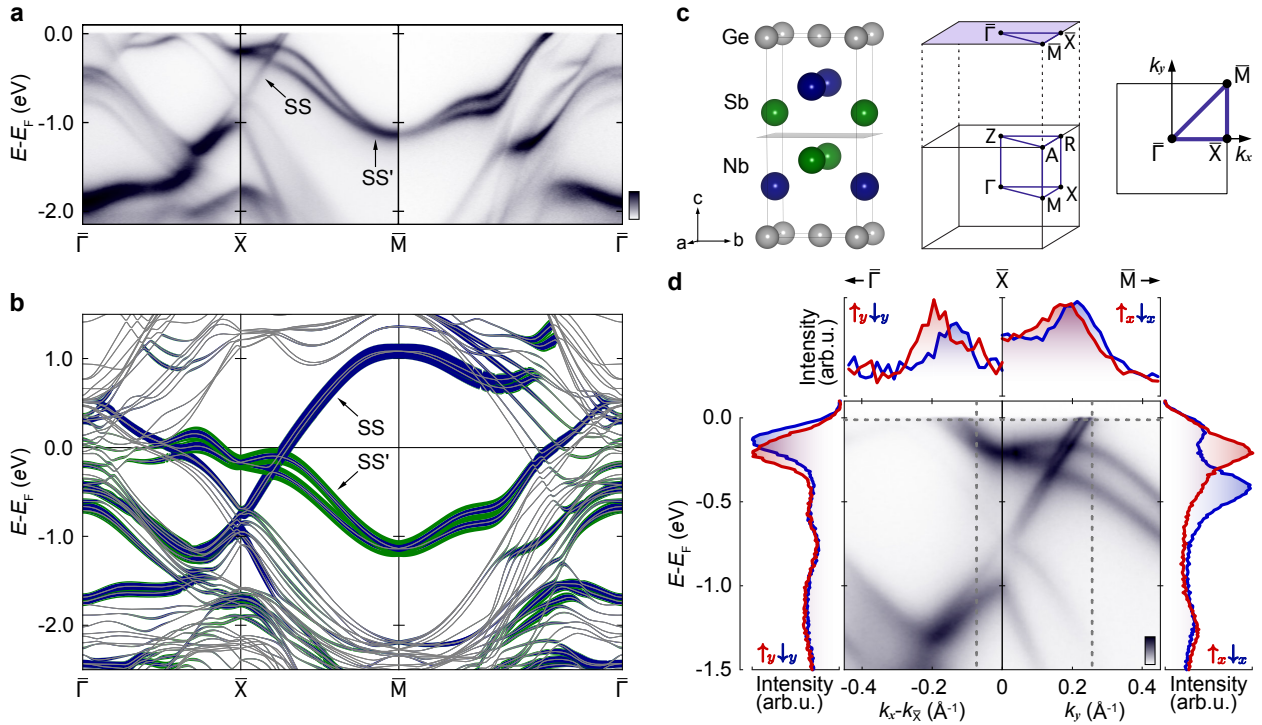


FIG. 1. **Spin-polarised surface electronic structure of NbGeSb.** (a) ARPES dispersions along the high-symmetry lines of the surface-projected Brillouin zone of NbGeSb. (b) Corresponding DFT slab calculation, with line colour and weight representing the wavefunction projection onto the surface Nb (blue) and Sb (green) atoms. (c) Crystal structure of NbGeSb with its primary cleavage plane shown; the bulk and surface projected Brillouin zones are also shown. (d) ARPES measurements in the vicinity of the \bar{X} point. A clear splitting of each set of surface states is visible and spin-resolved energy (EDC) and momentum (MDC) distribution curves (shown left/right and top) show this to be a spin splitting. The spin quantisation axis is normal to the high-symmetry line along which the measurement is performed.

37 large k_z -projected band gaps in the surface Brillouin zone (see also Supplementary Fig. S1).
 38 As compared to ZrSiS, the two manifolds of surface states have been strongly shifted towards
 39 each other, in fact to such an extent that they now cross through each other in the vicinity
 40 of the Fermi level.

41 Our measurements and calculations indicate a clear splitting of each surface state into
 42 two branches away from the high-symmetry (time-reversal invariant momentum) \bar{X} and \bar{M}
 43 points. Spin-resolved energy (EDC) and momentum (MDC) distribution curves (Fig. 1(d))
 44 reveal a clear spin polarisation of these surface states, where the measured spin projection
 45 reverses sign between the upper and lower split-off branches of each surface state. We
 46 attribute this surface state spin splitting to the Rashba effect²⁵, whereby spin degeneracy
 47 is lifted by spin-orbit coupling when inversion symmetry is broken at the surface. The
 48 magnitude of the induced spin splitting is large, reaching up to ~ 225 meV for the SS'
 49 manifold close to the \bar{X} point (Fig. 1(d)).

50 The corresponding surface state spin texture is also strongly constrained by the high
 51 symmetry of the surface unit cell (Fig. 2(a)). Its C_4 rotational symmetry, combined with
 52 time-reversal symmetry, immediately precludes any out-of-plane spin canting. Moreover,
 53 the $\bar{\Gamma} - \bar{X}$, $\bar{X} - \bar{M}$, and $\bar{\Gamma} - \bar{M}$ directions are all mirror lines. Along such lines, all non-
 54 degenerate states must be eigenstates of the mirror operator, constraining the spin to lie
 55 perpendicular to these mirror lines, fully consistent with our experimental measurements
 56 (see also Supplementary Fig. S2). Governed by these constraints, the resulting surface state
 57 Fermi surface develops a highly structured spin texture, as shown schematically in Fig. 2(b).

58 **Surface state band crossings**

59 This Fermi surface is already a product of the intertwining of the two sets of surface
 60 states: the Fermi crossing along $\bar{X} - \bar{\Gamma}$ is from the SS' surface state, while that along
 61 $\bar{X} - \bar{M}$ is from the SS state (Fig. 1(d)). Indeed, in contrast to ZrSiS where the surface state
 62 electron pocket smoothly shrinks with increasing binding energy⁹, here a complex evolution
 63 of the constant energy contours is observed (Supplementary Fig. S3), showing a succession
 64 of Lifshitz-like transitions as the surface states pass through each other. Along the high-
 65 symmetry $\bar{X} - \bar{M}$ line, a quartet of band crossings is formed where the two pairs of surface
 66 states disperse through each other (Fig. 2(c)). Two are between bands which have the same

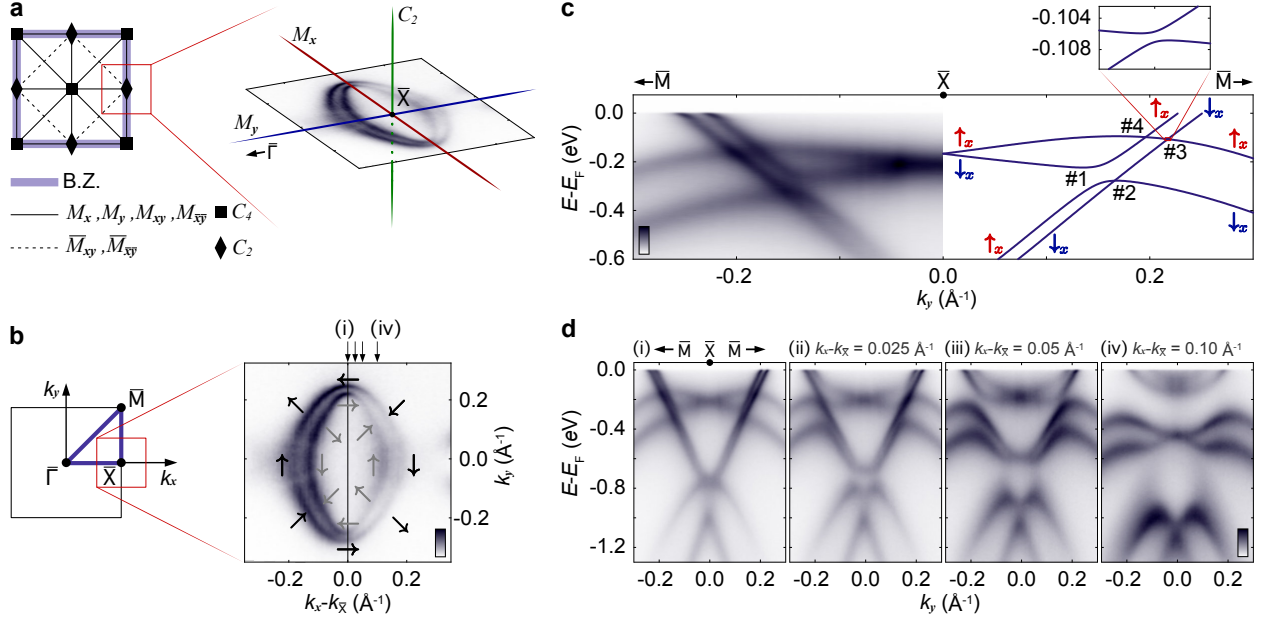


FIG. 2. **Mirror-symmetry protected surface band crossings.** (a) Symmetry elements of the $p4mm$ layer group²⁶, which applies to the surface projected Brillouin zone and the surface unit cell of NbGeSb. The inset shows the relevant symmetries at the \bar{X} point overlaid on the surface state Fermi surfaces measured in the vicinity of this point. (b) The resulting spin textures of these Fermi surfaces are shown schematically by arrows. (c) High-resolution ARPES measurements (left) and DFT calculations (right) in the vicinity of the surface state crossings along $\bar{X} - \bar{M}$. The four band crossings are numbered and spin polarisation is again indicated by arrows. Inset is a close-up of crossing #3, showing a small hybridisation gap of ca. 1 meV. (d) ARPES dispersions measured off the $\bar{X} - \bar{M}$ line, along the cuts indicated in (b), demonstrating the evolution of the crossing structure away from the M_x mirror line at the Brillouin zone edge.

67 spin polarisation as each other (crossings #2 and #4 in Fig. 2(c)), and two are between
68 bands with opposite spin polarisation (crossings #1 and #3 in Fig. 2(c)). Intriguingly, our
69 measurements indicate that there is negligible band hybridisation at three of the crossing
70 points, while crossing #1, between oppositely spin-polarised states, develops a pronounced
71 hybridisation gap on the order of 50 meV. DFT calculations performed on a very dense \mathbf{k} -
72 grid (inset of Fig. 2(c)) indicate that the crossing between opposite-spin states that appears
73 to be protected experimentally (#3) in fact opens a very small band gap. This is, however,
74 on the order of only 1 meV, too small to be resolved experimentally here, and a factor of ca.
75 50 times smaller than the gap opening at the nearby partner crossing. In contrast, clearly

76 resolvable hybridisation gaps open at all four crossing points when off the high-symmetry
 77 line (Fig. 2(d)), indicating a critical role of the mirror symmetry which is present along the
 78 Brillouin zone boundary (Fig. 2(a)) in generating the structure observed here.

79 The strongly asymmetric nature of the hybridisation structure along the mirror line is
 80 highly unusual: for a conventional bulk state where the orbital degree of freedom is quenched
 81 by the crystal field, there is no *a priori* reason to distinguish between the $(\downarrow_x, \uparrow_x)$ and $(\uparrow_x, \downarrow_x)$
 82 crossings, and comparable hybridisation matrix elements would be expected at both. The
 83 presence of inversion symmetry breaking at the surface, however, allows additional orbital hy-
 84 bridisations which can drive the development of unquenched orbital angular momentum²⁷⁻³¹.

85 Along the mirror line, the surface eigenstates must have definite mirror parity^{17,32}. This
 86 is evident in our DFT slab calculations shown with the wavefunction weight projected onto
 87 atomic orbital basis states of the surface layer atoms (Supplementary Fig. S4). Along $\bar{X} - \bar{M}$,
 88 the SS band consists only of orbitals that are even under M_x , which form the basis for the
 89 orbitally unquenched states with $L_x = \{-2, 0, +2\}$. In contrast, the SS' band is composed
 90 only of orbitals which are odd under M_x , forming the basis for $L_x = \{-1, +1\}$. The
 91 OAM states of the two bands thus belong to orthogonal manifolds. Further insight into the
 92 OAM structure can be gained from the magnitude of the spin splitting. In particular, the
 93 maximum size of the observed spin splittings here (~ 90 meV for SS and ~ 225 meV for SS',
 94 Fig. 2(c)) are comparable to the average of the atomic spin-orbit coupling of Nb 4d and Sb 5p
 95 orbitals^{33,34} weighted by their relative contribution to the band. This points to the energy
 96 scale associated with inversion symmetry breaking being greater than the atomic spin-orbit
 97 coupling strength³¹. As such, a pronounced OAM can be expected here, with approximately
 98 the same expectation value for each of the spin-split branches of a given surface state²⁹⁻³¹.

99 **Orbital angular momentum**

100 To explore this further, we construct a simple tight-binding model based on a symmetry
 101 analysis of the allowed inter-orbital hopping terms for the NbGeSb surface structure (see
 102 Methods). The full band dispersions from this model are shown in Supplementary Fig. S5,
 103 while we focus here on the $\bar{X} - \bar{M}$ direction (Fig. 3(a)) for which a similar structure of two
 104 protected and two asymmetrically gapped crossings arises to that observed experimentally
 105 for NbGeSb. Fig. 3(b) shows the resulting OAM which develops for these surface bands.

106 Just as for the spin angular momenta, mirror symmetry constrains the OAM to point per-
 107 pendicular to the mirror line; along the M_x mirror line shown here, only the perpendicular
 108 OAM component, L_x , can therefore develop. In line with the above considerations based
 109 on the magnitude of the spin splitting observed experimentally, both spin-split branches of
 110 the SS' surface state develop a similar OAM, which we find is very close to a pure $L_x = 1$
 111 state (Fig. 3(b)). Both branches of the SS surface state are close to $L_x = 0$, although the
 112 small, but non-zero, expectation value of the OAM indicates that this band additionally
 113 hosts some admixture of $L_x = \pm 2$.

114 As a good starting approximation, we neglect the small admixture of $L_x = \pm 2$ and
 115 consider the SS and SS' bands to be purely in neighbouring levels of the underlying OAM
 116 manifold (i.e. $L_x = 0$ and $L_x = 1$, respectively). The resulting minimal model of the
 117 four surface band crossings is that of a two-level system for both spin and orbital angular
 118 momenta, as shown schematically in Fig. 3(c). Along the mirror lines, only atomic spin-orbit
 119 coupling of the $\mathbf{L} \cdot \mathbf{S}$ form can open a hybridisation gap at the band crossings, as inter-orbital
 120 mixing between the states of opposite mirror parity is otherwise strictly forbidden. The
 121 atomic spin-orbit coupling is naturally represented in the x basis as $\mathbf{L} \cdot \mathbf{S} = L_x S_x + \frac{1}{2}(L_+ S_- +$
 122 $L_- S_+)$ ³⁵, due to the pinning of both spin and orbital angular momenta perpendicular to the
 123 mirror line.

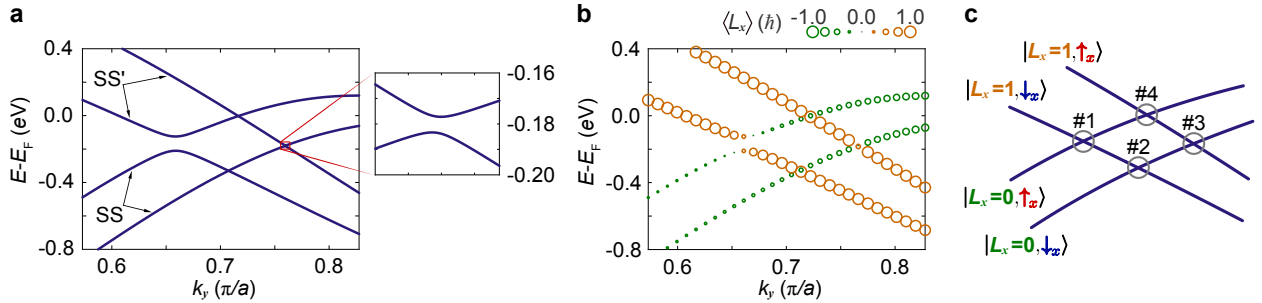


FIG. 3. **Orbital angular momentum of the surface states.** (a) The fourfold crossing of the SS and SS' surface states in our tight-binding model (see Methods). A magnified view of crossing #3 is shown inset. (b) Reproduction of the tight-binding dispersions from (a), with the calculated expectation value of the orbital angular momentum along the x quantisation axis shown as symbol colour/size. (c) Schematic of the fourfold crossing of SS and SS' surface states. The crossings are numbered as in Fig. 2(c), and ket labels on the bands represent the orbital and spin angular momenta of the bands in our minimal model.

124 The “spin-flip” terms (last two terms) connect states for which the angular momentum
 125 change of the spin is opposite to that of the orbital sector. This is the situation only
 126 for crossing #1 here, which thus opens a clear hybridisation gap, as observed for the real
 127 material (Fig. 2(c)). In contrast, at crossing #3, between $|L_x=1, \uparrow_x\rangle$ and $|L_x=0, \downarrow_x\rangle$ states,
 128 the spin-flip terms cannot act because the angular momentum change of the spin is of the
 129 same sign as that of the orbital sector. Moreover, the $L_x S_x$ term cannot act at any of
 130 the crossings because the states have different L_x projection at all of these. Within our
 131 minimal model, crossing #3 is therefore protected. In reality, the admixture of $L_x = \pm 2$
 132 into SS removes this strict protection by allowing a contribution from the spin-flip terms.
 133 The resulting hybridisation gap will, however, naturally be much smaller than at crossing
 134 #1, explaining the highly asymmetric nature of the hybridisation gap structure observed
 135 for NbGeSb. In the tight-binding example shown in Fig. 3(a), the gap at crossing #3 is
 136 14 times smaller than that at crossing #1, while an even larger ratio is found for the real
 137 material (Fig. 2(c)), indicating that deviations from the effective two-level system employed
 138 in Fig. 3(c) are small in reality.

139 At the like-spin crossings, #2 and #4, the spin-flip terms of the atomic spin-orbit coupling
 140 cannot act because the spin projection in each band is the same, while the $L_x S_x$ term again
 141 cannot act because the states have different L_x projection. This remains true even including
 142 deviations from pure OAM eigenstates, because the spin is still polarised along x for states
 143 along the mirror line, and the orbital angular momentum states of the two bands belong
 144 to strictly orthogonal manifolds. These crossings are thus strictly protected by the defined
 145 mirror parity of the bands.

146 **Generation of Weyl-like points**

147 Moving off the Brillouin zone boundary, inter-orbital mixing and spin canting become
 148 allowed, and so the crossing points along the mirror line represent isolated band degenera-
 149 cies. Fig. 4(a) shows the resulting band dispersions in the vicinity of one of these protected
 150 crossings (#4). This has the characteristic form of a type-I tilted Weyl cone known from
 151 three-dimensional solids³⁶, but now confined to a two-dimensional surface layer. Conven-
 152 tionally, stabilising Weyl points is assumed to require three dimensions in order to tune
 153 all hybridisation terms to zero: in two dimensions, a perturbation of σ_z type would thus

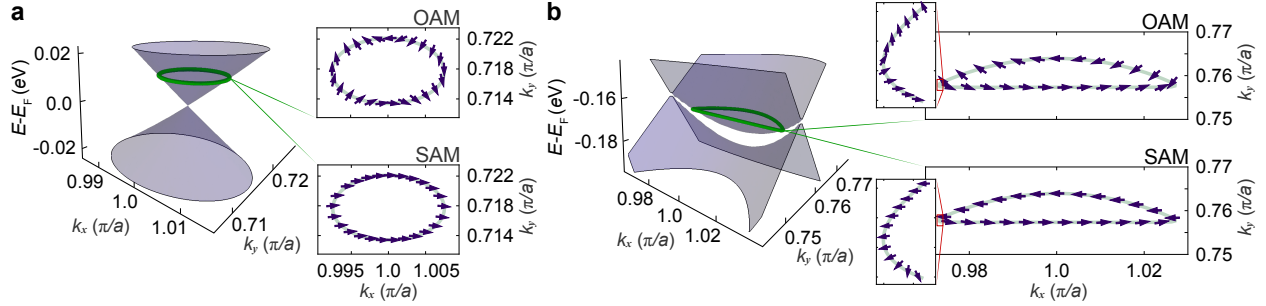


FIG. 4. **Weyl-like points in the surface band structure of NbGeSb.** (a) Band dispersions around the like-spin protected crossing (#4 from Fig. 3(c)) as calculated from our tight-binding model. Orbital (top) and spin (bottom) angular momenta extracted around the indicated contour are shown as insets; the arrows represent the direction of the angular momenta. The OAM shows a characteristic winding around the contour with winding number -1 , unlike for the spin which exhibits only slight canting around the contour. (b) Equivalent calculations around the weakly gapped crossing (#3 in Fig. 3(c)). Now both the orbital (top inset) and spin (bottom inset) angular momenta exhibit winding around the indicated contour, with winding numbers -1 and $+1$ respectively, but the majority of the winding is restricted in close proximity to the mirror line, as can be seen in the magnified insets.

154 generically be expected to open a band gap in the quasiparticle spectrum. Here, the mirror
 155 symmetry at the Brillouin zone edge provides a key additional symmetry constraint, prevent-
 156 ing such hybridisations and allowing the realisation of Weyl-like points from band inversions
 157 of two-dimensional surface states. This is reminiscent of the situation in black phosphorus,
 158 where surface doping with alkali metals was recently shown to modify the bulk band struc-
 159 ture so as to drive a band inversion in the near-surface region, with Dirac states stabilised
 160 by glide-mirror symmetry³⁷. Here, however, rather than arising via surface modification of
 161 the bulk states, it is the inherent surface states of the material which themselves exhibit
 162 an intrinsic band inversion. Moreover, a strong spin-orbit coupling means that the band
 163 crossings occur between spin-polarised states, as identified above, leading to the generation
 164 of Weyl-like rather than Dirac-like states.

166 At the protected crossings, the two bands which intersect have the same spin polarisation
 167 as each other, but different orbital angular momentum parity. In contrast to a conventional
 168 Weyl cone, the spin texture here thus exhibits no winding, but rather only a weak canting

169 around the cone (Fig. 4(a) - bottom right). Instead, it is the orbital angular momentum that
 170 winds, in order to interpolate between the two opposite parities as one goes round a small
 171 loop in \mathbf{k} -space around the crossing point (Fig. 4(a) - top right). The chiral pseudospin of
 172 the analogue Weyl cones which form is therefore derived from their OAM, with the effective
 173 low-energy Hamiltonian given by a 2×2 matrix of the Weyl form: $H_{\text{eff}} = v \xi_z (\tau_x p_y + \tau_y p_x)$
 174 (see Methods), where \mathbf{p} is the in-plane momentum measured relative to the crossing point, v
 175 is a velocity, τ is an orbital pseudospin, and ξ_z is a pseudospin-1/2 variable describing which
 176 zone face the crossing is on. We thus denote these crossings as Weyl-like⁵. At the weakly
 177 gapped crossing #3, the two bands have opposite spin polarisation as well as different orbital
 178 angular momentum parity. Both the spin and the orbital angular momentum therefore
 179 exhibit winding (Fig. 4(b)), leading to an arguably even richer entanglement of the spin and
 180 orbital degrees of freedom. This winding would be present even if the gap induced by the
 181 $\mathbf{L} \cdot \mathbf{S}$ spin-orbit term were to close.

182 DISCUSSION

183 The above findings illustrate how surface states, as well as bulk states, can provide a rich
 184 environment for realising, and indeed extending, the rich variety of electronic structures that
 185 can be generated from band inversions in solids, opening new opportunities to profit from the
 186 different symmetries and environment of the surface itself. Further theoretical work is needed
 187 to ascertain whether the Weyl cone analogues observed here would in principle support long-
 188 lived one dimensional edge states. More generally, it may be possible to stabilise such edge
 189 states as the boundary modes of parity-inverted surface state band gaps, even if the bulk
 190 of the material is itself topologically trivial. This would provide an interesting alternative
 191 to hinge-state systems³⁸⁻⁴⁰, where 1D edge modes are also created, but as a result of a
 192 higher-dimensional bulk topological invariant.

193 For NbGeSb studied here, the simultaneous presence of bulk states crossing the Fermi
 194 level close to the Brillouin zone centre would complicate the observation of signatures of
 195 the surface Weyl-like cones or corresponding edge states in, for example, transport measure-
 196 ments. Nonetheless, the observations from surface-sensitive spectroscopy here motivate the
 197 future search for new materials where the protected surface state crossings are tuned into
 198 a projected gap of the bulk electronic spectrum, and thus become accessible to transport.

199 In this regard, we note that surface state energies can often be more readily manipulated
200 than those of corresponding bulk states, for example via surface adsorption or even electrical
201 gating of interface states, providing greater opportunities for manipulating the underlying
202 surface electronic structure than are present for bulk states. The concept of surface band
203 inversions outlined here may therefore present a highly tunable platform for inducing and
204 manipulating topological and symmetry-protected surface electronic states of materials.

205 METHODS

206 Sample synthesis

207 High-quality NbGeSb single crystals (space group $P4/nmm$, no. 129)^{6,22} were grown via
208 chemical vapour transport using iodine as the transport agent by similar methods to those
209 described elsewhere⁴¹. Elemental Nb (Alfa Aesar 99.99%), Ge (Alfa Aesar 99.999%) and
210 Sb (Alfa Aesar 99.99%) were combined stoichiometrically in the molar ratio 1:1:1 under an
211 argon atmosphere and ground into a fine powder. Dry lumped iodine in the concentration
212 10 mg/cm³ was then added to the powder and both were sealed in a 20 cm quartz tube
213 under vacuum. The quartz tube was then kept in a two-zone gradient furnace for 336 hr
214 with the hot end at 850°C and the cooler end at 750°C. After cooling to room temperature,
215 shiny rod-like crystals were obtained at the cooler end and single crystal x-ray diffraction
216 confirmed growth of NbGeSb.

217 Angle-resolved photoemission

218 The samples were cleaved *in situ* at the measurement temperature of $\sim 10 - 20$ K.
219 Spin-integrated angle-resolved photoemission (ARPES) measurements were performed at
220 the CASSIOPEE beamline of Soleil synchrotron, France, while spin-resolved ARPES mea-
221 surements were performed utilising very low-energy electron diffraction (VLEED)-based spin
222 polarimeters⁴² at the BL-9B beamline of Hiroshima Synchrotron Radiation Center (HiSOR),
223 Japan⁴³, and at the APE beamline of Elettra synchrotron, Italy⁴⁴. The Sherman functions
224 were calibrated for the utilised targets via reference measurements of the surface states of
225 Bi(111) and Au(111) for BL-9B and APE respectively, and the data shown in Fig. 1(d) and
226 Fig. S1 has been normalised to account for this finite Sherman function. The dispersions

227 shown in Fig. 1(a) and Supplementary Fig. S2 were measured using $h\nu = 65$ eV circularly
228 polarised light; the data is shown as the sum of measurements performed using circular-left
229 and circular-right polarised light. All other photoemission data, both spin-integrated and
230 spin-resolved, was measured using $h\nu = 18$ eV linearly p -polarised light, except for the slices
231 shown in Fig. 2(d) and Supplementary Fig. S3 which are presented as the sum of measure-
232 ments performed using p - and s -polarised light in order to aid visibility of all of the band
233 features.

234 **Density-functional theory**

235 Electronic band structures were calculated using density functional theory (DFT). Plane-
236 wave based periodic calculations were performed using the VASP programme⁴⁵. Core-
237 electrons were treated using the projector-augmented wave method⁴⁶, with the exception
238 of Nb 4s, 4p and Ge 3d states which were treated as valence electrons. Calculations used
239 the PBE functional⁴⁷ with the inclusion of spin-orbit coupling⁴⁸. All calculations used a
240 plane-wave cutoff energy of 500 eV.

241 The cell parameters and atomic positions of bulk NbGeSb were optimised starting from
242 the experimentally reported crystal structure and using a grid of $20 \times 20 \times 9$ \mathbf{k} -points until
243 all forces fell below 0.001 eV/Å. A five unit cell thick slab of NbGeSb was then created by
244 repeating the relaxed bulk structure seven times in the c direction and removing two unit
245 cells such that the slab was symmetrically terminated by layers of Sb atoms. All atomic
246 coordinates were subsequently optimised within a fixed periodic cell, using a $20 \times 20 \times 1$
247 \mathbf{k} -point grid, until all forces were reduced to below 0.001 eV/Å. This generated a slab of
248 NbGeSb with a vacuum region of 18.36 Å separating the Sb surface layers in periodic images.
249 Subsequent calculations of the electronic structure at specific \mathbf{k} -points were performed non-
250 self-consistently using the electron density generated using the full $20 \times 20 \times 1$ \mathbf{k} -point grid.

251 **Tight-binding calculations**

252 To explore the physics of the surface band structure of NbGeSb in a controllable setting,
253 we created a tight-binding model for the electrons in the five d -orbitals of the surface Nb
254 atoms. Including symmetry-allowed mixings of the Sb orbitals would not influence any of

255 the essential understanding here, and so we neglect them for simplicity. The resulting tight-
 256 binding model thus has ten basis states per Nb atom: the orbitals $d_{3z^2-r^2}$, $d_{x^2-y^2}$, d_{yz} , d_{xy} ,
 257 and d_{xz} with spin-projection up, and the same orbitals with spin-projection down.

258 We build the Hamiltonian for this model in three stages,

$$H = H_0 + H_R + H_{\text{SO}} : \quad (1)$$

259 • First, we consider the spin-independent tight-binding hopping processes between
 260 nearby Nb atoms, H_0 . We use only relatively near-neighbour form factors: $c_+ \equiv$
 261 $\cos k_x + \cos k_y$; $c_- \equiv \cos k_x - \cos k_y$; $s_x \equiv i \sin k_x$; $s_y \equiv i \sin k_y$; and $s_{xy} \equiv \sin k_x \sin k_y$.
 262 The allowed form factors are constrained by the symmetries of the model: C_4 rota-
 263 tional symmetry, the mirror symmetries M_x and M_y , and time-reversal symmetry.
 264 The M_z mirror is not enforced, reflecting the fact that inversion symmetry is broken
 265 along z by the presence of the surface potential. Because the C_4 rotational symmetry
 266 mixes the d_{xz} and d_{yz} orbitals, it constrains certain elements of H_0 to have the same
 267 hopping integral as each other. We choose the remaining hopping integrals arbitrarily.
 268 The resulting Hamiltonian is

$$H_0 = \begin{pmatrix} \Delta_1 + t_1 c_+ & t_2 c_- & t_3 s_y & t_4 s_{xy} & t_3 s_x \\ t_2 c_- & \Delta_2 + t_5 c_+ & t_6 s_y & 0 & -t_6 s_x \\ -t_3 s_y & -t_6 s_y & \Delta_3 + t_7 c_+ + t_8 c_- & t_9 s_x & t_{10} s_{xy} \\ t_4 s_{xy} & 0 & -t_9 s_x & \Delta_4 + t_{11} c_+ & -t_9 s_y \\ -t_3 s_x & t_6 s_x & t_{10} s_{xy} & t_9 s_y & \Delta_3 + t_7 c_+ - t_8 c_- \end{pmatrix}, \quad (2)$$

269 and the parameters we have utilised are $\Delta_1 = \Delta_2 = -1$, $\Delta_3 = \Delta_4 = 0$, $t_1 = -0.5$,
 270 $t_2 = -0.75$, $t_3 = t_4 = t_5 = t_6 = -1$, $t_7 = 0.75$, $t_8 = 0.25$, $t_9 = 1$, $t_{10} = 0.3$, and
 271 $t_{11} = 0.5$.

272 • Second, we add Rashba spin-orbit coupling of the form $H_R = \alpha_R \hat{\mathbf{z}} \cdot (\mathbf{S} \times \mathbf{k})$ with $\alpha_R =$
 273 0.2 . This splits each band of H_0 into a pair of bands with opposite spin orientations,
 274 though the axis along which the spins are oriented is different in different points of
 275 the surface Brillouin zone.

276 • Third, we add intra-unit-cell spin-orbit coupling of the form $H_{\text{SO}} = \alpha_{\text{SO}} \mathbf{L} \cdot \mathbf{S}$ with
 277 $\alpha_{\text{SO}} = 0.02$. While in reality both H_R and H_{SO} originate from the same microscopic
 278 spin-orbit term in the real-space Hamiltonian, it is convenient to divide that term into
 279 an intra-unit-cell component H_{SO} (which is taken to be independent of the crystal
 280 momentum \mathbf{k}) and an inter-unit-cell component H_R ⁴⁹. This allows us to investigate
 281 the influence of orbital mixing generically allowed by the $\mathbf{L} \cdot \mathbf{S}$ term on the crossings
 282 generated by the Rashba term.

283 The band structure of the resulting model is shown in Supplementary Fig. S5. Near zero
 284 energy on the $\bar{X} - \bar{M}$ line it shows a crossing structure similar to that of NbGeSb, as
 285 reproduced in Fig. 3(a,b) of the main text. Notice, in particular, that without fine-tuning
 286 of the parameters of the tight-binding model we naturally obtain a very large asymmetry (a
 287 factor of around 14) between the size of the small and large gaps arising from the effect of
 288 H_{SO} at the unprotected crossings.

289 **Low-energy effective Hamiltonian**

290 It is clear from Fig. 4 that the orbital angular momentum in the bands has non-trivial
 291 winding around the protected crossing, just as the spin does in a conventional Weyl point.
 292 Since there are two bands involved, each with an orbital angular momentum that varies
 293 only slowly in the vicinity of the protected crossing, we may represent the orbital angular
 294 momentum using a pseudospin-1/2 variable $\boldsymbol{\tau}$ which has the same transformation properties
 295 under the spatial symmetries and time-reversal as the physical orbital angular momentum
 296 \mathbf{L} . The corresponding low-energy effective Hamiltonian, valid in the vicinity of the Weyl-like
 297 points, is

$$H_{\text{eff}} = v \xi_z (\tau_x p_y + \tau_y p_x). \quad (3)$$

298 Here \mathbf{p} is the in-plane momentum measured relative to the crossing point, v is a velocity,
 299 and ξ_z is a pseudospin-1/2 variable describing which zone face the crossing is on: $\xi_z = -1$
 300 for the face at $k_x a = \pi$ and $\xi_z = +1$ for the face at $k_y a = \pi$.

301 This effective Hamiltonian is invariant under the symmetries of the zone face:

302 • *Time reversal.* Under time reversal, both $\boldsymbol{\tau}$ and \mathbf{p} change sign, while $\boldsymbol{\xi}$ does not,
 303 leaving H_{eff} unchanged.

- 304 • *Mirrors.* Under the M_x mirror operation, τ_x and p_y are invariant, while τ_y and p_x
 305 change sign. Hence the term in parentheses is invariant overall; since ξ_z is also un-
 306 changed by M_x , H_{eff} is invariant under M_x . The same argument with x and y inter-
 307 changed demonstrates the invariance of H_{eff} under M_y .
- 308 • *C_4 rotation.* C_4 rotation makes the following changes:

$$\begin{aligned}
 p_x &\rightarrow p_y, & p_y &\rightarrow -p_x, \\
 \tau_x &\rightarrow \tau_y, & \tau_y &\rightarrow -\tau_x, & \xi_z &\rightarrow -\xi_z.
 \end{aligned}
 \tag{4}$$

309 Therefore the term in parentheses changes sign, but so does ξ_z , meaning that H_{eff} is
 310 invariant overall.

311

312 **Data availability.** The data that underpins the findings of this study are available at: *doi*
 313 *to be provided.*

314

315 **Acknowledgments.** We thank G. A. Fiete, A. P. Mackenzie, and V. Sunko for enlighten-
 316 ing discussions. We gratefully acknowledge The Leverhulme Trust (Grant No. PLP-2015-
 317 144), The Royal Society, and the Engineering and Physical Sciences Research Council, UK
 318 (Grant No. EP/R031924/1) for support. We are grateful to Soleil Synchrotron for access to
 319 beamline CASSIOPEE, Elettra Synchrotron for access to the APE beamline, and HiSOR
 320 Synchrotron for access to beamline BL-9B under the HiSOR Proposal No. 17BG022, which
 321 all contributed to this work, and the CALIPSOplus project under Grant Agreement 730872
 322 from the EU Framework Programme for Research and Innovation HORIZON 2020. I.M.
 323 acknowledges financial support by the International Max Planck Research School for Chem-
 324 istry and Physics of Quantum Materials (IMPRS-CPQM). O.J.C. and J.M.R. acknowledge
 325 EPSRC for studentship support through grant nos. EP/K503162/1 and EP/L505079/1.
 326 This work has been partly performed in the framework of the Nanoscience Foundry and
 327 Fine Analysis (NFFA-MIUR, Italy) facility. C.A.H. is grateful to Rice University for their
 328 hospitality during a four-month visiting professorship, where part of this work was carried
 329 out.

330

331 **Author contributions.** The experimental data were measured by I.M., O.J.C., F.M.,
332 M.D.W., J.M.R., K.V., K.U. and P.D.C.K., and analysed by I.M.. C.A.H. developed the
333 theoretical models in discussions with I.M. and P.D.C.K.. M.S.D. and P.A.E.M. performed
334 the DFT calculations. K.J.M. and J.A. synthesised the measured samples. P.L.F., F.B.,
335 J.F., I.V., S.W. and T.O. maintained the ARPES/spin-resolved ARPES end stations and
336 provided experimental support. I.M., P.D.C.K. and C.A.H. wrote the manuscript with input
337 and discussion from co-authors. P.D.C.K. was responsible for overall project planning and
338 direction.

339

340 **Competing financial interests.** The authors declare no competing financial interests.

-
- [1] Hasan, M. Z. & Kane, C. L. Colloquium. *Reviews of Modern Physics* **82**, 3045–3067 (2010).
- [2] Qi, X.-L. & Zhang, S.-C. Topological insulators and superconductors. *Reviews of Modern Physics* **83**, 1057–1110 (2011).
- [3] Armitage, N., Mele, E. & Vishwanath, A. Weyl and Dirac semimetals in three-dimensional solids. *Reviews of Modern Physics* **90**, 015001 (2018).
- [4] Yang, S.-Y. *et al.* Symmetry demanded topological nodal-line materials. *Advances in Physics: X* **3**, 1414631 (2018).
- [5] Vafeek, O. & Vishwanath, A. Dirac Fermions in Solids: From High-Tc Cuprates and Graphene to Topological Insulators and Weyl Semimetals. *Annual Review of Condensed Matter Physics* **5**, 83–112 (2014).
- [6] Haneveld, A. J. K. & Jellinek, F. Zirconium silicide and germanide chalcogenides preparation and crystal structures. *Recueil des Travaux Chimiques des Pays-Bas* **83**, 776–783 (1964).
- [7] Schoop, L. M. *et al.* Dirac cone protected by non-symmorphic symmetry and three-dimensional Dirac line node in ZrSiS. *Nature Communications* **7**, 11696 (2016).
- [8] Topp, A. *et al.* Surface Floating 2d Bands in Layered Nonsymmorphic Semimetals: ZrSiS and Related Compounds. *Physical Review X* **7**, 041073 (2017).
- [9] Chen, C. *et al.* Dirac line nodes and effect of spin-orbit coupling in the nonsymmorphic critical semimetals MSiS (M=Hf, Zr). *Physical Review B* **95**, 125126 (2017).
- [10] Ali, M. N. *et al.* Butterfly magnetoresistance, quasi-2d Dirac Fermi surface and topological

- phase transition in ZrSiS. *Science Advances* **2**, e1601742 (2016).
- [11] Hosen, M. M. *et al.* Tunability of the topological nodal-line semimetal phase in ZrSiX-type materials (X=S, Se, Te). *Physical Review B* **95**, 161101 (2017).
- [12] Hu, J. *et al.* Nearly massless Dirac fermions and strong Zeeman splitting in the nodal-line semimetal ZrSiS probed by de Haas–van Alphen quantum oscillations. *Physical Review B* **96**, 045127 (2017).
- [13] Pezzini, S. *et al.* Unconventional mass enhancement around the Dirac nodal loop in ZrSiS. *Nature Physics* **14**, 178 (2018).
- [14] Singha, R., Pariari, A. K., Satpati, B. & Mandal, P. Large nonsaturating magnetoresistance and signature of nondegenerate Dirac nodes in ZrSiS. *Proceedings of the National Academy of Sciences* **114**, 2468–2473 (2017).
- [15] Su, C.-C. *et al.* Surface termination dependent quasiparticle scattering interference and magneto-transport study on ZrSiS. *New Journal of Physics* **20**, 103025 (2018).
- [16] Wang, X. *et al.* Evidence of Both Surface and Bulk Dirac Bands and Anisotropic Nonsaturating Magnetoresistance in ZrSiS. *Advanced Electronic Materials* **2**, 1600228 (2016).
- [17] Dresselhaus, M. S., Dresselhaus, G. & Jorio, A. *Group Theory - Application to the Physics of Condensed Matter* (Springer-Verlag Berlin Heidelberg, 2008).
- [18] Young, S. M. & Kane, C. L. Dirac Semimetals in Two Dimensions. *Physical Review Letters* **115**, 126803 (2015).
- [19] Nica, E. M., Yu, R. & Si, Q. Glide reflection symmetry, Brillouin zone folding, and superconducting pairing for the P4/nmm space group. *Physical Review B* **92**, 174520 (2015).
- [20] Neupane, M. *et al.* Observation of topological nodal fermion semimetal phase in ZrSiS. *Physical Review B* **93**, 201104 (2016).
- [21] Takane, D. *et al.* Dirac-node arc in the topological line-node semimetal HfSiS. *Physical Review B* **94**, 121108 (2016).
- [22] Johnson, V. & Jeitschko, W. PbFCl-type pnictides of niobium with silicon or germanium. *Journal of Solid State Chemistry* **6**, 306–309 (1973).
- [23] Tremel, W. & Hoffmann, R. Square nets of main-group elements in solid-state materials. *Journal of the American Chemical Society* **109**, 124–140 (1987).
- [24] Lv, Y.-Y. *et al.* Extremely large and significantly anisotropic magnetoresistance in zrsis single crystals. *Applied Physics Letters* **108**, 244101 (2016).

- [25] Bychkov, Y. & Rashba, E. I. Properties of a 2d electron gas with lifted spectral degeneracy. *JETP Letters* **39** (1984).
- [26] Hahn, T. (ed.) *International tables for crystallography. Vol. A: Space-group symmetry* (Springer, 2005).
- [27] Park, S. R., Kim, C. H., Yu, J., Han, J. H. & Kim, C. Orbital-Angular-Momentum Based Origin of Rashba-Type Surface Band Splitting. *Physical Review Letters* **107**, 156803 (2011).
- [28] Park, J.-H., Kim, C. H., Rhim, J.-W. & Han, J. H. Orbital Rashba effect and its detection by circular dichroism angle-resolved photoemission spectroscopy. *Physical Review B* **85**, 195401 (2012).
- [29] Kim, B. *et al.* Microscopic mechanism for asymmetric charge distribution in Rashba-type surface states and the origin of the energy splitting scale. *Physical Review B* **88**, 205408 (2013).
- [30] Park, S. R. & Kim, C. Microscopic mechanism for the Rashba spin-band splitting: Perspective from formation of local orbital angular momentum. *Journal of Electron Spectroscopy and Related Phenomena* **201**, 6–17 (2015).
- [31] Sunko, V. *et al.* Maximal Rashba-like spin splitting via kinetic-energy-coupled inversion-symmetry breaking. *Nature* **549**, 492–496 (2017).
- [32] Tinkham, M. *Group Theory and Quantum Mechanics*. International Series in Pure and Applied Physics (McGraw-Hill Book Company, 1964).
- [33] Herman, F. & Skillman, S. *Atomic Structure Calculations* (Prentice-Hall, Inc., 1963).
- [34] Wittel, K. & Manne, R. Atomic spin-orbit interaction parameters from spectral data for 19 elements. *Theoretica chimica acta* **33**, 347–349 (1974).
- [35] Sakurai, J. J. *Modern Quantum Mechanics* (Benjamin-Cummings, 1985).
- [36] Soluyanov, A. A. *et al.* Type-II Weyl semimetals. *Nature* **527**, 495–498 (2015).
- [37] Kim, J. *et al.* Two-Dimensional Dirac Fermions Protected by Space-Time Inversion Symmetry in Black Phosphorus. *Physical Review Letters* **119**, 226801 (2017).
- [38] Schindler, F. *et al.* Higher-order topological insulators. *Science Advances* **4**, eaat0346 (2018).
- [39] Benalcazar, W. A., Bernevig, B. A. & Hughes, T. L. Quantized electric multipole insulators. *Science* **357**, 61–66 (2017).
- [40] Song, Z., Fang, Z. & Fang, C. (d-2)-Dimensional Edge States of Rotation Symmetry Protected Topological States. *Physical Review Letters* **119**, 246402 (2017).

- [41] Sankar, R. *et al.* Crystal growth of Dirac semimetal ZrSiS with high magnetoresistance and mobility. *Scientific Reports* **7** (2017).
- [42] Okuda, T., Miyamoto, K., Kimura, A., Namatame, H. & Taniguchi, M. A double VLEED spin detector for high-resolution three dimensional spin vectorial analysis of anisotropic Rashba spin splitting. *Journal of Electron Spectroscopy and Related Phenomena* **201**, 23–29 (2015).
- [43] Okuda, T. *et al.* Efficient spin resolved spectroscopy observation machine at Hiroshima Synchrotron Radiation Center. *Review of Scientific Instruments* **82**, 103302 (2011).
- [44] Bigi, C. *et al.* Very efficient spin polarization analysis (VESPA): new exchange scattering-based setup for spin-resolved ARPES at APE-NFFA beamline at Elettra. *Journal of Synchrotron Radiation* **24**, 750–756 (2017).
- [45] Kresse, G. & Furthmüller, J. Efficient iterative schemes for ab initio total-energy calculations using a plane-wave basis set. *Physical Review B* **54**, 11169–11186 (1996).
- [46] Kresse, G. & Joubert, D. From ultrasoft pseudopotentials to the projector augmented-wave method. *Physical Review B* **59**, 1758–1775 (1999).
- [47] Perdew, J. P., Burke, K. & Ernzerhof, M. Generalized gradient approximation made simple. *Physical Review Letters* **77**, 3865–3868 (1996).
- [48] Steiner, S., Khmelevskiy, S., Marsmann, M. & Kresse, G. Calculation of the magnetic anisotropy with projected-augmented-wave methodology and the case study of disordered $\text{Fe}_{1-x}\text{Co}_x$ alloys. *Physical Review B* **93**, 224425 (2016).
- [49] Adams, E. N. Magnetic Susceptibility of a Diamagnetic Electron Gas—The Role of Small Effective Electron Mass. *Physical Review* **89**, 633–648 (1953).

Supplementary Material: Weyl-like points from band inversions of spin-polarised surface states in NbGeSb

I. Marković,^{1,2} C. A. Hooley,¹ O. J. Clark,¹ F. Mazzola,¹ M. D. Watson,¹ J. M. Riley,¹ K. Volckaert,¹ K. Underwood,¹ M. S. Dyer,³ P. A. E. Murgatroyd,⁴ K. J. Murphy,⁴ P. Le Fèvre,⁵ F. Bertran,⁵ J. Fujii,⁶ I. Vobornik,⁶ S. Wu,⁷ T. Okuda,⁸ J. Alaria,⁴ and P. D. C. King¹

¹*SUPA, School of Physics and Astronomy,
University of St Andrews, St Andrews KY16 9SS, United Kingdom*

²*Max Planck Institute for Chemical Physics of Solids,
Nöthnitzer Strasse 40, 01187 Dresden, Germany*

³*Department of Chemistry, University of Liverpool,
Liverpool L69 7ZD, United Kingdom*

⁴*Department of Physics, University of Liverpool,
Liverpool L69 7ZE, United Kingdom*

⁵*Synchrotron SOLEIL, CNRS-CEA, L'Orme des Merisiers,
Saint-Aubin-BP48, 91192 Gif-sur-Yvette, France*

⁶*Istituto Officina dei Materiali (IOM)-CNR,
Laboratorio TASC, Area Science Park,
S.S.14, Km 163.5, 34149 Trieste, Italy*

⁷*Graduate School of Science, Hiroshima University,
1-3-1 Kagamiyama, Higashi-Hiroshima 739-8526, Japan*

⁸*Hiroshima Synchrotron Radiation Center,
Hiroshima University, 2-313 Kagamiyama,
Higashi-Hiroshima 739-0046, Japan*

(Dated: November 21, 2019)

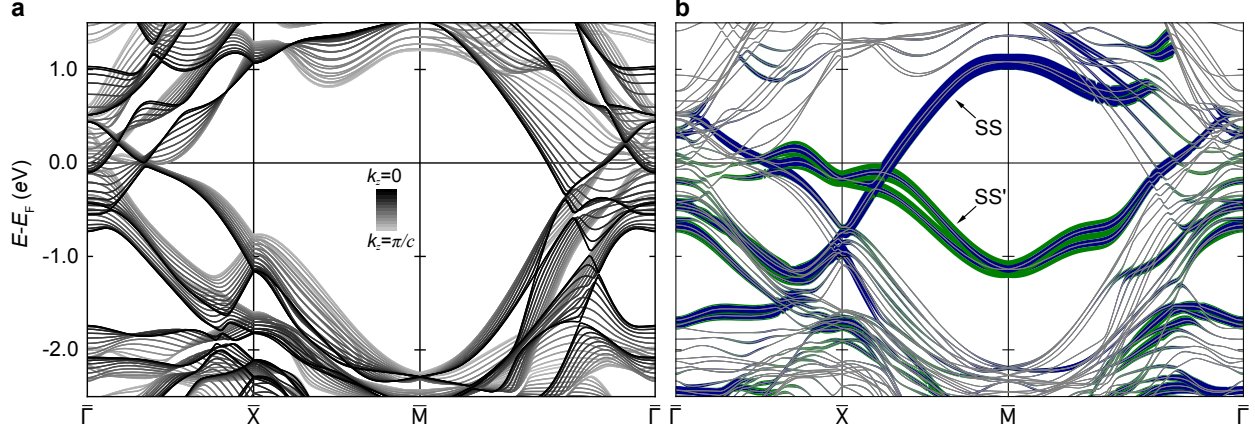


FIG. S1. **Bulk and surface calculated band structure of NbGeSb.** A side-by-side comparison of (a) a series of k_z -projected bulk DFT band structure calculations and (b) the DFT surface slab calculation reproduced from Fig. 1 of the main text. The grey colours in (a) indicate the value of the out-of-plane momentum, while line colours and weight in (b) represent the wavefunction projection onto the surface Nb (blue) and Sb (green) atoms, indicating the surface character of the states. From comparison of the two calculations, it is clear that SS and SS' are well-defined surface states where they disperse along the $\bar{X} - \bar{M}$ line, but become resonant with the bulk states in other portions of the Brillouin zone (e.g. close to $\bar{\Gamma}$).

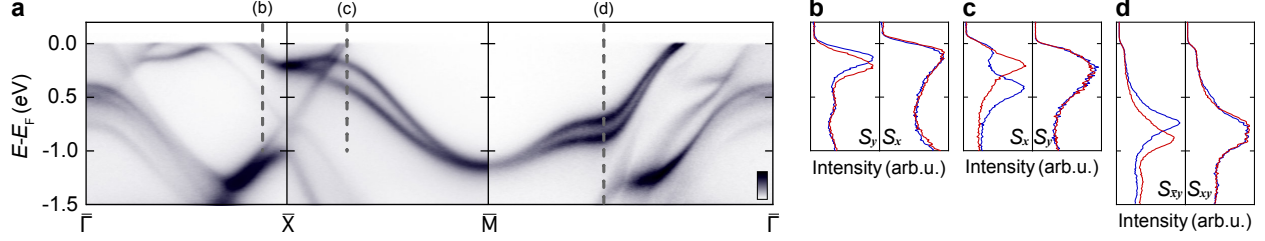


FIG. S2. **Spin polarisation of surface states along the high-symmetry lines of NbGeSb.**

(a) ARPES dispersions along the high-symmetry lines of the surface projected Brillouin zone of NbGeSb (as in Fig. 1(a) of the main text) with indicated positions where spin-resolved data was taken. (b-d) Spin-polarised energy distribution curves (EDC) along the lines indicated in the dispersions. For each cut we show spin-resolved data for the spin component perpendicular and parallel to the corresponding high-symmetry line. We observe a complete extinction of the surface state spin component parallel to the high-symmetry line as per the symmetry considerations presented in the main text. A consequence of these symmetry constraints is that these surface states must necessarily have a spin polarisation of 100% away from the hybridisation points where small band gaps open. From fitting our experimental EDCs, we extract spin polarisations of ca. 70-90% for the surface bands under study here. While this is lower than the complete spin polarisation necessitated by symmetry, we note that this is a multi-orbital system, of the form where inter-orbital photoelectron interference processes are known to influence the quantitative degree of spin polarisation that is observed in a SARPES experiment¹. Consequently, our experimental measurements are consistent with the conclusion of 100% spin polarisation in the initial states that is assumed in our modelling utilised in the main text, as also supported by our *ab initio* calculations.

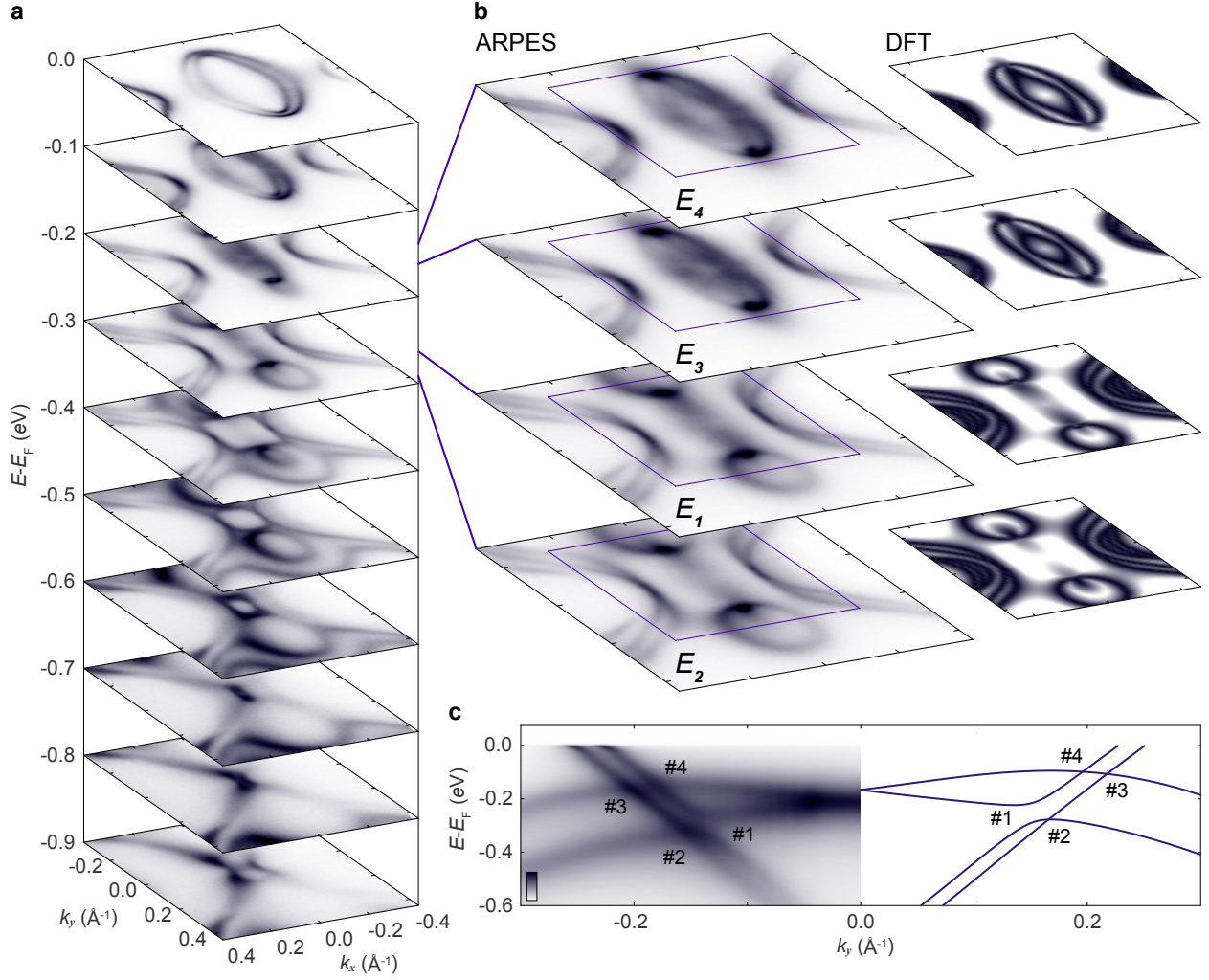


FIG. S3. **Surface state electronic structure around \bar{X} .** (a) Constant energy contours showing the evolution of the surface state Fermi pockets at \bar{X} with binding energy. (b) Selected constant energy contours shown at the binding energies $E_1 - E_4$ of the four points (#1 – #4) where the SS and SS' surface states cross along the Brillouin zone edge as determined from ARPES experiments (left) and DFT calculations (right). (c) The surface state band structure along the $\bar{X}-\bar{M}$ line, showing the four band crossings in question in a measured ARPES dispersion (left) and DFT calculation (right).

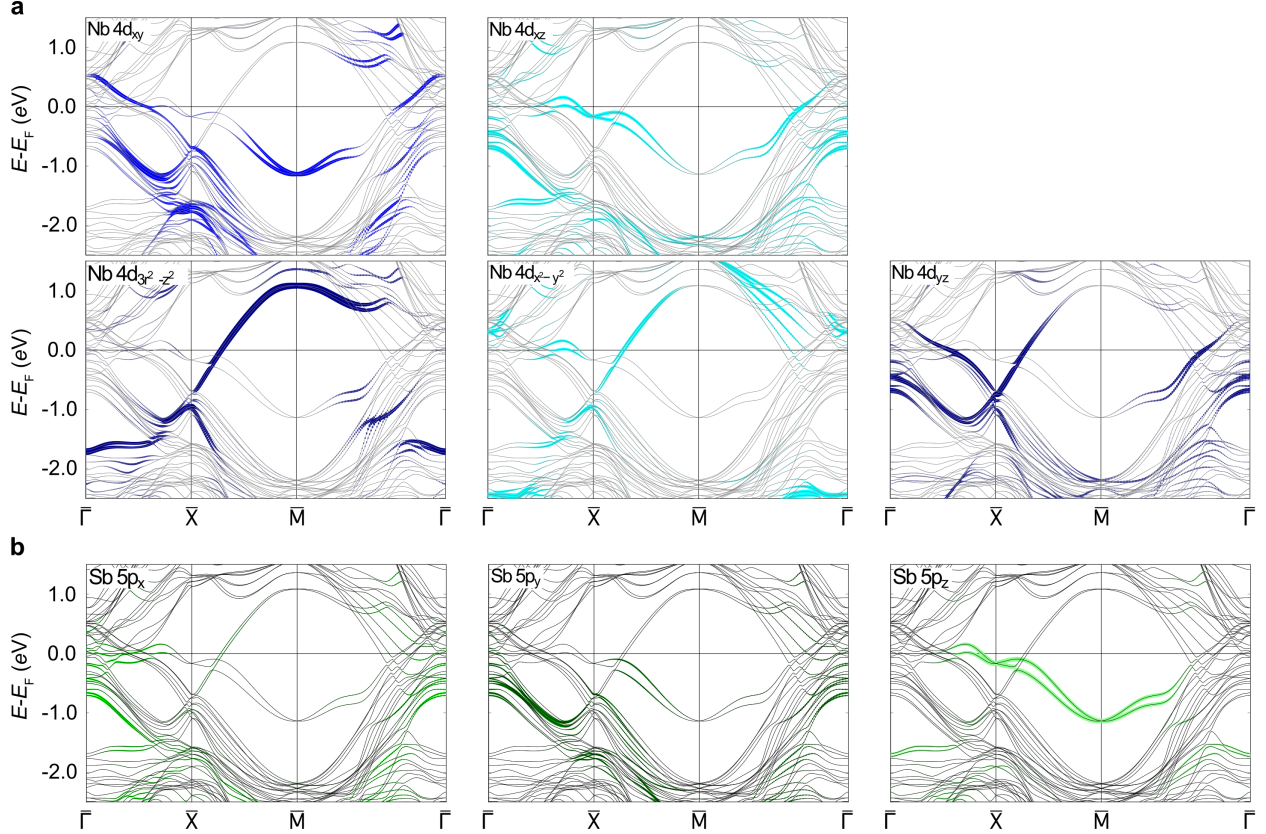


FIG. S4. **Orbital character of the surface states.** Surface slab calculations of the electronic structure from density-functional theory along the high-symmetry lines, projected onto (a) the surface Nb $4d$ -orbital manifold and (b) the Sb $5p$ -orbital manifold. The existence of the M_x mirror symmetry means that any non-degenerate state on the relevant \bar{X} - \bar{M} line must be an eigenstate of that symmetry, i.e. either even or odd under the transformation $x \rightarrow -x$. Nb orbital content of the bands (a) along the \bar{X} - \bar{M} line clearly satisfies this requirement: SS contains only those orbitals that are even under M_x , viz. $d_{3z^2-r^2}$, $d_{x^2-y^2}$, and d_{yz} (bottom row), while SS' contains only those that are odd, viz. d_{xy} and d_{xz} (top row). SS' also has significant Sb p_z -orbital content. Since p_z is even under M_x , that would appear to violate the above rule. It does not, however, because of additional Bloch phase factors that are incurred when M_x acts on the Sb orbitals. These arise because there is no M_x mirror plane that contains both the Nb and Sb atoms. Therefore, if we choose a mirror plane that leaves the Nb sites undisturbed, it will necessarily translate the Sb sites, and a compensating translation — with the associated Bloch factor $e^{i\mathbf{k}\cdot\mathbf{r}}$ — is necessary to bring them back to their original positions. The translation vector is $\mathbf{r} = (a, 0)$, where a is the Bravais lattice spacing; and on the \bar{X} - \bar{M} line we have $k_x = \pi/a$. Therefore the Bloch factor is $e^{i\pi} = -1$, which means that those orbitals of Sb that are naïvely even under M_x are in fact odd, and vice versa.

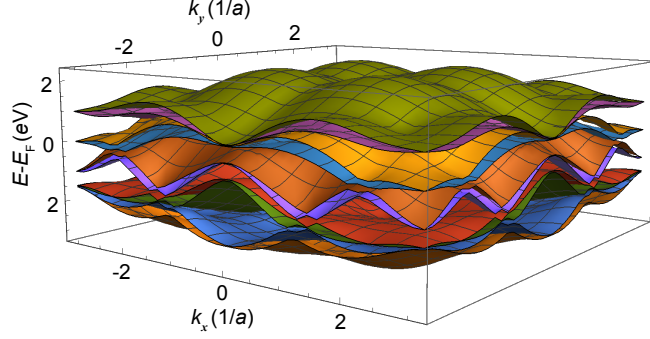


FIG. S5. **Full 5-orbital tight-binding model.** The tight-binding model was based on the five Nb $4d$ orbitals including spin. While relevant crystalline symmetries impose restrictions to certain hopping integrals of the Hamiltonian, the others were chosen arbitrarily, setting the spin-independent part of the Hamiltonian. We then add a Rashba spin-orbit coupling term, and finally an intra-unit-cell spin-orbit coupling term, $\mathbf{L} \cdot \mathbf{S}$. The model has spectator bands in the same energy range as the relevant surface state pairs, but still reproduces a crossing structure along the Brillouin zone edges similar to that of NbGeSb, which is reproduced in Fig. 3(a,b) and Fig. 4 of the main text. In reality, the other states of this manifold in NbGeSb are pushed further away in energy and become resonant with projected bulk bands. For more details on the tight-binding model, see the Methods section of the main text.

-
- [1] Zhu, Z.-H. *et al.* Layer-By-Layer Entangled Spin-Orbital Texture of the Topological Surface State in Bi_2Se_3 . *Physical Review Letters* **110**, 216401 (2013).